ACCEPTED MANUSCRIPT

A Deterministic Breakdown Model for Dielectric Interfaces Subjected to Tangential Electric Field

A Deterministic Breakdown Model for Dielectric Interfaces Subjected to Tangential Electric Field

Emre Kantar[a,b,*], Sverre Hvidsten[b]

[a]*Department of Electric Power Engineering, NTNU, O.S. Bragstads Plass 2E, 7491 Trondheim, Norway*
[b]*SINTEF Energy Research, Sem Sælands vei 11, 7034 Trondheim, Norway*

Abstract

The contact area between solid insulations, namely solid-solid interfaces, affect the dielectric characteristics of an entire insulation system. With the theoretical and experimental studies covered in this paper, we intend to investigate the effects of the elastic modulus, interface contact pressure, and surface smoothness/roughness on the tangential AC breakdown strength (BDS) of contact surfaces at dielectric interfaces that undergo a tangential electric field. Four distinct solid dielectric specimens with various elastic modulus values were employed. The interfaces between the same materials were subjected to AC breakdown and partial discharge (PD) tests at different contact pressure values. In addition, the interface surfaces were polished using four different sandpapers of various grits to scrutinize the effect of surface roughness. A deterministic model built around the tribology of solid surfaces was proposed to determine the sizes of the interfacial cavities and to simulate the 3D displacement and deformation of the surface protrusions based on the surface roughness, contact pressure, elastic modulus, and hardness of an interface. The estimated sizes of cavities and contact areas were then coupled with a comprehensive breakdown model that addressed the cavity discharge and breakdown of contact areas, separately. The results by the model were correlated with the results of the AC breakdown and PD experiments to elucidate not only how cavities were linked at solid-solid interfaces but also the effects of roughness, elasticity, contact pressure, and gas pressure inside of the cavities.

Keywords: Deterministic contact model, elastic-plastic contact, electrical breakdown, polymer, solid-solid interface.

1. Introduction

Electrical insulation systems incorporate various insulating and conductive materials. In the majority of high-voltage (HV) systems, the electrical insulation system consists of the series connection of two or more dielectrics. The lowest alternating current (AC) breakdown strength (BDS) of a bulk insulation or an interfaces between neighboring insulating materials determine the overall BDS of an insulation system. When two nominally flat surfaces make contact, the real surface is not perfectly smooth, and the real contact at the interface is not ideal as well, leading to numerous microcavities (used interchangeably with cavity) between adjacent contact spots [1–3].

Cavities may undergo partial discharges (PD) that may lead to interfacial tracking and a premature electrical breakdown (BD) [4, 5]. Besides, the dielectric media inside of the cavities affects the PD inception field strength thereof [6, 7]. An interface, hence, is a weak region likely to lessen the tangential AC BDS of an HV insulation system due to local electric field enhancements occurring in the cavities [4–6, 8].

Scholars have mainly investigated the electrical and chemical features of dielectric materials with regards to the BDS of bulk, surface flashover and tracking, insula-tion degradation without investigating the solid-solid interfaces separately. Few studies have focused on the interfacial HV insulation performance between two solid dielectrics [4, 5, 8]. It was reported that the elasticity and surface roughness of the solid materials, dielectric medium surrounding the interfaces, and contact/interfacial pressure are the primary determinants affecting the dielectric strength of an interface. Also, the authors' previous studies, concerning the tangential AC BDS of solid interfaces [7, 9, 10], demonstrated significant dependencies on these factors. However, neither the mechanisms governing the electrical interfacial BD nor the correlation between the shape/size, number of cavities (size of contact area) and the interfacial BD has yet been fully understood.

Kato et al. [8] examined the correlation between the pressure distribution and the interfacial AC BD voltage. Though their experimental results were in line with the above-mentioned literature, they highlighted the need for realistic modeling of the deformation of microcavities between two solid dielectrics to further explain the correlation between the interfacial morphology and the interfacial BDS. The authors' previous work [10, 11] also demonstrated the need for an intricate 3D interface contact model.

To that end, in this paper, the interfacial topographies at different contact pressures, roughnesses, and elastic moduli were studied by employing both theoretical

---
*Corresponding author.
Email address: emre.kantar@sintef.no (Emre Kantar)

modeling and experimental testing. Firstly, AC BD and PD experiments under different interface pressures, roughness levels, and elasticities were conducted. Subsequently, a deterministic model was adapted based on the material properties used in the experiments to simulate the 3D deformation of the surface protrusions as functions of the contact pressure, surface smoothness/roughness, elastic modulus, and hardness of an interface. To provide the deterministic model with the real 3D surface data, we characterized the morphology of the polished sample surfaces using a 3D-optical profilometer. Using the model, the sizes and densities of the cavities and the real area of contact, under the same conditions as in the experiments, were examined. The estimated sizes of the cavities and contact areas were then integrated with a comprehensive electrical breakdown model that addressed the cavity discharge and breakdown of contact areas, separately. Finally, the correlation between the results of the AC breakdown/PD experiments and the BD model was analyzed.

2. A Deterministic Contact Model for Asperities and Contact Spots at Solid-Solid Interfaces

In this work, the deterministic roughness model proposed by Almqvist [12] based on the Tian and Bhushan's model [13] was modified to simulate the effects of the contact pressure, surface roughness, elasticity, and material hardness on the 3D deformation of the surface asperities at solid-solid interfaces employed in HV insulation systems.

The developed model elucidates how cavities are connected at solid-solid interfaces and enables the estimation of the gas pressure inside the resulting cavities. The model is built on the "equivalent rough surface approach", where the contact between two rough surfaces has been shown to be negligibly different from the equivalent rough surface (consisting of a perfectly smooth and an equivalent rough surface) [1, 14–17], as illustrated in Fig. 1. It comprises linear elastic and perfectly plastic contacts, where the energy dissipation owing to plastic deformation is taken into consideration.

The contact model requires the real 3D topography (profile) of the interfacial surfaces. The model adopts the "theory of minimum potential complementary energy" when simulating a contact surface, i.e., the interface between two surfaces. The pressure distribution and the deformation of peaks and valleys of the 3D profile under the given conditions are determined by finding the minimum value of an integral equation (with respect to potential energy) in respect of the applied contact pressure and material properties. The output of the deterministic model is a deformed surface based on the computed displacements of real, measured surface profiles. That is to say, it is a simulated 3D profile of the contact surface between a perfectly smooth plane and the measured surface profile. At the contact surface (interface), the sizes of all cavities and total area of contact are definite.

The 3D surface profile of the polished samples (forming a solid-solid interface) were measured using a 3D-optical
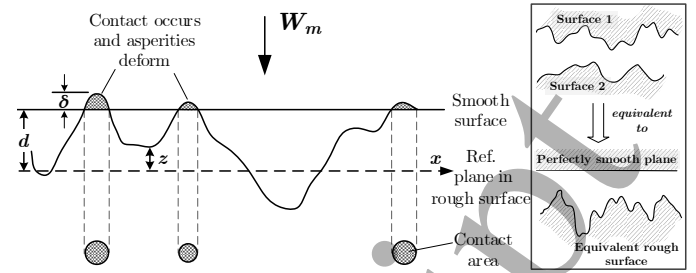

Fig. 1: Illustration of a contact surface between an equivalent rough surface and a perfectly smooth surface (reference plane) [11].

profilometer and fed into the deterministic model. In this work, this procedure is referred to as "simulation" as in "simulated results/interfaces/deformations", or "interface simulations." Details on the implementation of the variational principle and the solution methods for the interface simulations are provided in Appendix A.1–A.3.

2.1. Equations to Define the Mechanical Contact Problem

The surface deformation and contact pressure distribution are determined by the variational problem defined in Eqs. (1)-(2), allowing 2D or 3D topographies. Total complementary potential energy, F is minimized using a nested iterative process by finding a p_a value that leads to $\nabla F = 0$, by taking the energy dissipation due to plastic deformations into account [2, 12, 13]:

$$\min_{0 \le p_a \le H_s} (F) = \min_{0 \le p_a \le H_s} \left(\frac{1}{2} \int_\Omega p_a \, \delta_e \, d\Omega - \int_\Omega p_a \, (h_2 - h_1 - \delta_p) \, d\Omega \right), \tag{1}$$

$$\int_\Omega p_a \, d\Omega = \iint_\Omega p_a \, dx \, dy = W_m \,, \tag{2}$$

where Ω is an arbitrary area, H_s represents the hardness of the softer solid (in the case of two different materials forming an interface), p_a is the contact pressure, $\delta_e = z - d$ is the elastic deformation with reference to Fig. 1, $h_g = h_2 - h_1$ is the gap between the undeformed surfaces, δ_p is the amount of plastic deformation, and W_m is the applied load. Eq. (1) is limited by two main constraints such that the maximum pressure is limited to the hardness of the softer material, i.e., $p_a \le H_s$, while it is assumed equal to or greater than zero. Thereby, for elastic contact spots, increased normal loads lead to the elevation of local contact pressure, resulting in larger real contact area whereas contact area no longer changes with respect to load in perfectly plastic contacts [2, 12, 13].

For two elastic half-spaces, the amount of deflection of elastic surface $\delta_e(x)$ at a given pressure is expressed as [2, 12, 13]:

$$\delta_e(x) = \int_{-\infty}^{\infty} K(x - s) \, p_a(s) \, ds + C \,, \tag{3}$$

where C is an arbitrary integral constant, and the kernel function K is provided by [12]:

$$K\left(x-s\right) = -\frac{4}{\pi E'}\ln\left|x-s\right|, \qquad (4a)$$

$$K\left(x_1 - s_1,\, x_2 - s_2\right) =$$
$$-\frac{2}{\pi E'}\frac{1}{\sqrt{\left(x_1 - s_1\right)^2 + \left(x_2 - s_2\right)^2}}, (4b)$$

for 2D and 3D contacts, respectively. E' stands for the composite (equivalent) elastic modulus of the two contacting solids, incorporating the elastic modulus of each material in contact ξ, calculated by:

$$\frac{2}{E'} = \frac{1 - v_1^2}{\xi_1} + \frac{1 - v_2^2}{\xi_2}, \qquad (5)$$

where ξ_1, ξ_2 are elastic modulus, and v_1, v_2 are Poisson's ratio of each material, respectively [2, 12, 13].

2.2. Representation of Numerical Data

The results of the deterministic model are displayed using contour plots. Contour lines in this work represent the amplitudes of the asperities as well as the area of cavities and contact spots at a solid-solid interface, as illustrated in Fig. 2. Different levels are represented by different colors, where red indicates the highest peak, and light yellow indicates the zero level.
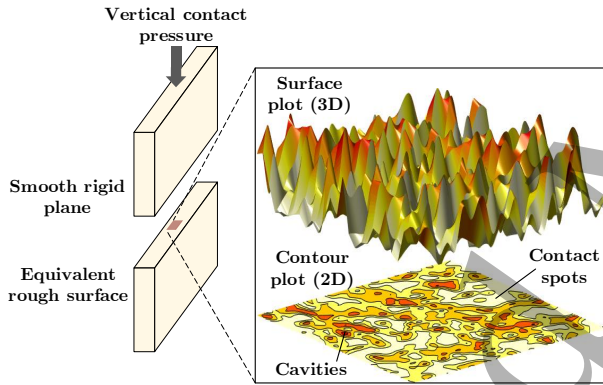

Fig. 2: Illustration of contact between a perfectly smooth surface and a rough sum surface with colored-contour lines representing the surfaces with planes at different amplitudes. Rectangular samples represent the specimens used in the experiments (see Fig. C.1).

3. Estimation of the Tangential AC Breakdown Strength of Solid-Solid Interfaces

The shape, size, and number of cavities and contact spots strongly affect the breakdown strength of an interface. Since the dielectric strength of a gas-filled cavity is notably lower than that of bulk insulation, PD activity can be presumed to start in the cavities first [18]. Our previous studies have suggested that discharged cavities do not necessarily lead to an interface breakdown immediately [7, 9, 10]. Interfacial tracking/PD resistances of the insulation materials, forming an interface, determine the endurance of the contact spots against breakdown [19–22]. Therefore, we hypothesized that the electrical breakdown of a solid-solid interface should incorporate not only the

discharge of air-filled cavities but also the breakdown of contact spots enclosing those cavities [10].

Cavities and contact spots connected in series comprise the electrical breakdown model of an interface along which the applied voltage is distributed, as illustrated in Fig. 3:

$$V_{app} = \sum_{j=1}^{n} V_{cav_j} + \sum_{k=1}^{m} V_{cnt_k}, \qquad (6)$$

where V_{app} is the applied voltage across the dry interface, n and m is the total number of cavities and contact spots, respectively, V_{cav_j} is the voltage drop across the jth cavity, and V_{cnt_k} is the voltage drop across the kth contact spot, as illustrated in Fig. 3. Equation (6) can be rearranged to be represented by the electric field strength and the size of each cavity and contact spot:

$$E_{app}\, d_{int} = \sum_{j=1}^{n} E_{cav_j}\, d_{cav_j} + \sum_{k=1}^{m} E_{cnt_k}\, l_{cnt_k}, \qquad (7)$$

where E_{app} is the applied nominal field strength at the interface, d_{int} is the nominal thickness of the interface, E_{cav_j} is the electric field across the jth cavity, E_{cnt_k} is the electric field across the kth contact spot. The contact spots in the model stand for ideal void-free contact areas in which d_{cav_j} and l_{cnt_k} denote the sizes of jth cavity and k^{th} contact spot in the field direction, respectively.
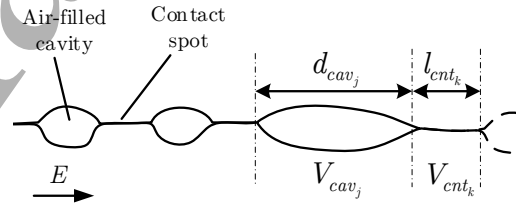
Fig. 3: 2D illustration of an interface (cavities and contact spots). Voltage drops at the cavities and contact spots are illustrated where E is the electric field strength in the tangential direction.

The interface breakdown model, thus, incorporates two submodels consisting of a model for the discharge of cavities and a model for the breakdown of contact spots. The deterministic model proposed in this work was used to develop the submodel for the cavity discharge: It estimates the PD inception field strength based on the estimated cavity size determined by the deterministic model based on the given elasticity, surface roughness, and contact pressure. In other words, E_{cav} and d_{cav} values are estimated using the cavity discharge model. Similarly, to estimate the values of E_{cnt} and l_{cnt}, the other submodel was employed: The empirical model presented in [10] was used for the breakdown of contact spots, based on the interfacial tracking resistance of solid materials (where enhanced field strengths at the edges of discharged cavities were approximated by a needle-needle electrode configuration). As the cavity discharge submodel is predicated upon the deterministic model proposed in this work, it is shown in the next section while the details of the submodel for the contact spot breakdown (theory and analytical expressions to

derive E_{cnt} and l_{cnt}) are provided in Appendix B in order for the main body of this paper to contain merely the newly introduced part.

3.1. Estimation of the Discharge Inception Field Strength of Air-filled Cavities

Under a homogeneous electric field, the cavity discharge inception field or, analogously, partial discharge inception field, PDIE of an air-filled cavity (E_{cav}) can be estimated using the well-known Paschen's law [7, 23]. The minimum value of PDIE is correlated with the critical avalanche length (longest path) in the field direction [24–26]. Therefore, as the electric field within a cavity can be represented by three orthogonal vectors, the axis parallel to the field (tangential component) will be adequate. Interfacial cavities arise in two different forms: enclosed or vented channels. The density of each are determined by the elasticity, contact pressure, and surface roughness. In the case of very large cavities and vented channels, initially compressed air is assumed to be squeezed out and is vented to the surroundings [10, 27]. Paschen's law suggest that the PDIE of vented cavities and channels, where the gas pressure inside the cavity (p_c) remains at the ambient pressure ($p_c \approx 1$ bar), is significantly lower than that of enclosed cavities where $p_c > 1$ bar.

Regarding the size of the cavities arising at the interfaces in the light of the experimental and theoretical work, the right-side of Paschen minimum, which covers cavity sizes from 10 µm to 1 mm, is considered in this work [11].

The PD inception field of a cavity, E_{cav} at a given pressure is analytically denoted by the polynomial fit:

$$E_{cav}\left(p_c, d_{cav}\right) = A\,\frac{p_0/p_c}{d_{cav}^2} + B\,\frac{p_c}{p_0} + \frac{C}{d_{cav}} + D\sqrt{\frac{p_c/p_0}{d_{cav}}}\,, \quad (8)$$

where d_{cav} is the cavity size in the field direction, p_c is the gas pressure inside the cavity, p_0 is atmospheric pressure (≈ 1 bar), $A = 0.00101$ kV $\cdot$ mm, $B = 2.4$ kV/mm, $C = -0.0097$ kV, $D = 2.244$ kV $\cdot$ mm$^{-0.5}$ [23]. The analytical expression suggests a reduced PDIE versus increased cavity size at a given p_c. Since the permittivity of air is less than the permittivity of the bulk material,

the electric field strength in air-filled cavities is enhanced in the field direction by the enhancement factor f:

$$f = \frac{\gamma\,\varepsilon_{r_i}}{1 + (\gamma - 1)\,\varepsilon_{r_i}}\,, \quad (9)$$

where ε_{r_i} is the relative permittivity of the material (contact spots), and γ is the shape factor varying as a function of the cavity geometry [28]. γ varies based on the ratio of the axis parallel to the field to the axis normal to the field. For spherical cavities, $\gamma = 3$, whereas for ellipsoidal cavities elongated in the field direction, $\gamma \geq 50$ [24].

The estimated PDIE, i.e., PDIE^e stands for the field strength at the interface (bulk insulation) (E_{int}[1]), calculated by dividing the value read from the Paschen's curve by the enhancement factor f:

$$\text{PDIE}^e = E_{int} = E_{cav}/f. \quad (10)$$

3.2. Sequence of Mechanisms Contributing to Breakdown under AC Ramp Excitation

The duration of electrical breakdown of an interface (referred to as "interfacial breakdown" hereafter), from no discharge activity to a complete flashover, is dissected in four consecutive periods. Therefore, cavity discharge and breakdown of contact spots will be initiated at different instants in a sequence, as illustrated in Fig. 4. The expected activity occurring in each period is described below:

1) *No PD*: This is the period from the application of the AC voltage until the *instant I* in Fig. 4. The electric field is not sufficiently strong to accelerate a free electron to start an avalanche mechanism in the cavities or absence of free electrons cause the delay of PD inception. Thus, no PD activity is observed in this period.

2) *Onset of PDs*: From the *instant I* onward, the electric field is sufficiently high to initiate a persistent discharge activity in the cavities (Fig. 4). However, the breakdown of contact spots does not occur as yet, because the interfacial tracking resistance of the contact spots can withstand the locally enhanced fields. Thus, only PD occurs in the largest cavities, perhaps in the smaller ones as well based on the simplified model shown in Fig. 3. (Refer to Fig. B.1 for the simulated interfacial field distribution.)

3) *Initiation and propagation of the interfacial tracking*: It is represented by the *instant II*. As mentioned above, the submodel for the interfacial tracking mechanism is operative at higher local electric fields with a BD time of around 10^{-7} s. Therefore, it takes only a fraction of a microsecond from the inception of an interfacial tracking to a breakdown of the contact spots between two discharged cavities.

4) *Breakdown of the interface*: The electrodes are bridged, and the destructive effects of the interfacial breakdown are clear at the material surfaces (as shown in Fig. 15).

Fig. 4: Activation sequence of the mechanisms with respect to the applied AC ramp voltage. Roman numerals, I and II stand for *instant I* and *instant II*, as referred to in the text [10].

---

[1]**Important note:** The conventional abbreviation, PDIE, is modified here, where PDIE^e stands for the estimated PDIE values at the interface described in this section. PDIE^m, on the other hand, will later be defined to represent the experimentally measured PDIE values at the interfaces.
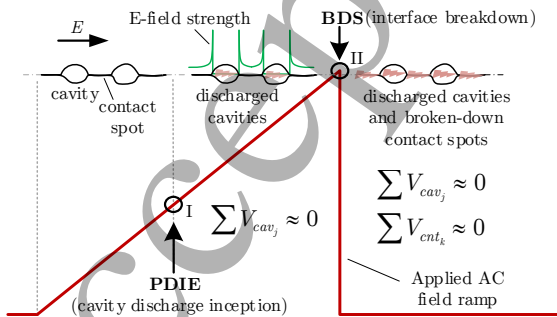
4. Experimental Procedure

To test the tangential AC BDS of solid-solid interfaces as a function of elasticity, we assembled four different interfaces at dry conditions using four different materials with different elastic moduli. The interfaces were formed between the same materials: cross-linked polyethylene (XLPE), epoxy, polyether ether ketone (PEEK), and silicone rubber (SiR) under various contact pressures applied by means of different mechanical loads (XLPE–XLPE, PEEK–PEEK, and so on).[2] The samples were cut/molded in rectangular prisms (4 mm × 55 mm × 30 mm), and two samples were positioned vertically on top of each other between two Rogowski-shaped electrodes, forming a 4-mm-long interface.

We prepared the contact surfaces of the specimens using a sanding machine and fixed the specimens in a revolving disk and positioned round sandpaper on the rotating plate [9]. To scrutinize the effect of surface roughness on the tangential AC interfacial BDS, XLPE samples of four different surface roughnesses were used. #180 (roughest)-, #500-, #1000-, and #2400 (smoothest)-grit sandpapers were used to prepare XLPE samples of various surface roughnesses. In the elastic modulus experiments, all samples were polished using #500-grit sandpaper (surface roughness was kept constant).

The determined contact pressure ranges for the interfaces were: SiR–SiR at 0.16–1.27 MPa, XLPE–XLPE at 0.5–1.67 MPa, EPOXY–EPOXY and PEEK–PEEK at 1.16–3.34 MPa (refer to Appendix C for the reasoning behind). For the AC breakdown tests, we subjected all samples to a homogeneous AC electric field using a 50-Hz AC ramp voltage at the rate of 1 kV/s until breakdown. The same type of AC voltage ramp of 1 kV/s was applied in the PD tests. Please refer to Appendix C for the details.

5. Results

5.1. AC Breakdown Experiments

In [10], we studied the effect of the elastic modulus on the tangential AC BDS of solid-solid interfaces between the same materials (SiR–SiR, XLPE–XLPE, EPOXY–EPOXY, and PEEK–PEEK) at various interfacial contact pressures with all the samples sanded using the same #500-grit sandpaper (7.8 μm mean asperity height [9]). For the sake of completeness, the results are summarized here as they will later be correlated with the output of the proposed model. The nominal 63.2 % values for each interface are shown in [10] with the corresponding 90 % CI values. The results demonstrated that higher elastic

modulus led to decreased BDS values. To elaborate, for the lowest elastic modulus (SiR–SiR), augmented contact pressure by a factor about 3 resulted in increased interfacial BDS values by a factor of 1.4, while the BDS value in the case of the highest modulus (PEEK–PEEK) was found to be 2.4 times as high. To sum up, materials with relatively low elastic moduli, e.g., SiR and XLPE, yielded increased BDSs even at relatively low pressures.

We also investigated the effect of the surface roughness on the tangential AC BDS of solid-solid interfaces between XLPE surfaces at 0.5, 0.86, and 1.16 MPa contact pressures in [9], where we presented the obtained 63.2 % BDS values with their 90 % CIs versus the sandpaper grit at each interface (using bar graphs to represent the arithmetic mean height S_a of the asperities calculated using the real 3D surface data). The interfacial BDS reduced as the surface roughness was increased whereas higher contact pressure led to a higher BDS. The 63.2 % BDS values of XLPE–XLPE #2400 ($S_a = 0.26$ μm) was about double the BDS values of XLPE–XLPE #180 ($S_a = 8.86$ μm) at each contact pressure. The data from both studies ([9, 10]) will be shown alongside the estimated results in Section 6.

5.2. AC Partial Discharge Experiments

Fig. 5 shows the measured PDIE^m results using the cumulative probability of Weibull distribution. Fig. 5 indicates that 63.2 % PDIE^m in the case of XLPE–XLPE #500 is higher than that of the PEEK–PEEK #500 at 1.16 MPa by a factor of 2.3. In the case of PEEK–PEEK #500 interface, increased pressure from 1.16 MPa to 2.25 MPa has also increased the 63.2 % PDIE^m by a factor of 1.8 while the 63.2 % PDIE^m augmented by a factor of 1.6 in the case of XLPE–XLPE #500. These results agree with the observations from the AC breakdown experiments although the extent of PD experiments is limited compared to that of AC breakdown experiments. In the AC breakdown experiments, BDS decreased at higher elastic modulus. In accordance with this finding, in the PD tests, XLPE–XLPE #500 has yielded higher PDIE^m compared to the PEEK–PEEK #500.
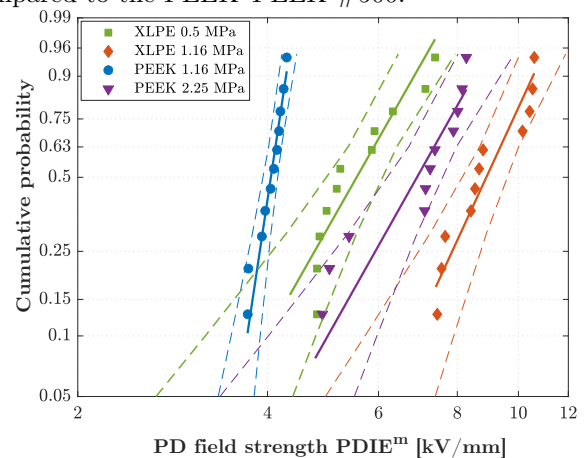
Fig. 5: Measured PDIE values of dry-mate XLPE–XLPE #500 and PEEK-PEEK #500 interfaces (cumulative Weibull plots with 90 % CIs). This figure is an extended version of the one presented in [10].

---

[2] Alternatively, elastic modulus could be varied by adding micro- and nano-scaled particles such as zinc oxide, zirconia, and silica, yet, adding such fillers causes as significant a change in the chemical/electrical properties as does selecting a different polymer [10]. Therefore, we chose materials widely-used in power cables and accessories and studied the interfaces between the same materials to minimize the influence of any unforeseen/neglected chemical and electrical properties. The electrical and mechanical properties of each material is shown in the supplementary section in Table C.1.

5.3. Deterministic Roughness Model

The results of the deterministic model are displayed using contour plots. The details regarding the data representation are provided in Section 2.2. It is important to recollect that an interface between two rough surfaces was transformed into an interface between one perfectly smooth plane and one equivalent rough surface (sum surface of the roughnesses of both surfaces), as illustrated in 3D in Fig. 2. Moreover, the 3D surface topography was mapped on a 2D plane using contour lines with color bars displaying the amplitudes of the peaks quantitatively (see Fig. 6). Simulation results were run at two different contact pressures—the lowest and highest pressure values at which the samples were tested in the AC breakdown experiments (see Section 4). An exception was made in the case of XLPE by setting the highest pressure to the next higher level to simulate to what further extent cavities shrink, and hence the contact area increases.

5.3.1. Effects of Surface Roughness and Contact Pressure

The protrusions at the XLPE interfaces of four distinct surface roughnesses are depicted in Fig. 6 by filled-contour plots, while those of the PEEK samples with two different surface roughness degrees are presented in Fig. 7. The contour plots suggest that increased pressure pushes the asperity tips further, leading to the formation of new contact spots. As a result, more cavities are formed due to channels (large air vents) being broken into smaller channels and cavities. Towards smoother interfaces, the density of the peaks reduces considerably, and the impact of the increased pressure becomes even more discernible. Particularly in the case of XLPE #2400, there were only a few protruding peaks at the surface, while the rest of the surface seemed to be perfectly smooth.

5.3.2. Effects of Elastic Modulus and Contact Pressure

To present the effect of elasticity and contact pressure, the simulated deformation and displacement of the asperities of the XLPE and PEEK samples in 2D are shown in Fig. 8. The waveforms represent equivalent rough surfaces while the horizontal axes stand for perfectly smooth planes (no asperities hypothetically, as illustrated in Fig. 1). Thus, the areas between the adjacent contact spots are the cavities formed between the surfaces. The sizes of cavities in the PEEK samples in the direction of the tangential electrical field were larger than those of the XLPE samples despite having been sanded by the same #500 grit sandpaper. Compared to XLPE, larger cavities and longer air-gaps with higher amplitudes in the case of PEEK are also discernible in Figs. 6–7. To improve readability, a smaller section of the interface of XLPE is shown, i.e., 0.3 mm. Consequently, higher pressure pushes the asperity tips forward (vertically toward the smooth plane–horizontal axis), leading to the formation of new contact spots. As a result, large cavities/channels break into smaller cavities. The deformation of the asperity tips is simulated by pressing the equivalent rough surface against the perfectly smooth rigid plane (horizontal axis)

as more of the afloat asperities come into contact with the smooth surface, resulting in larger contact area, and hence smaller cavities.

Note that these profiles constitute a small portion of the complete surface data, as illustrated with the red rectangle in Fig. 2. The complete surface data set was excessively large to be demonstrated in a single graph. The unrevealed parts of the surfaces had similar, uniform patterns. As mentioned in Appendix A.2, complete 3D surface data is stored in a 480×1240 mesh, whereas a row
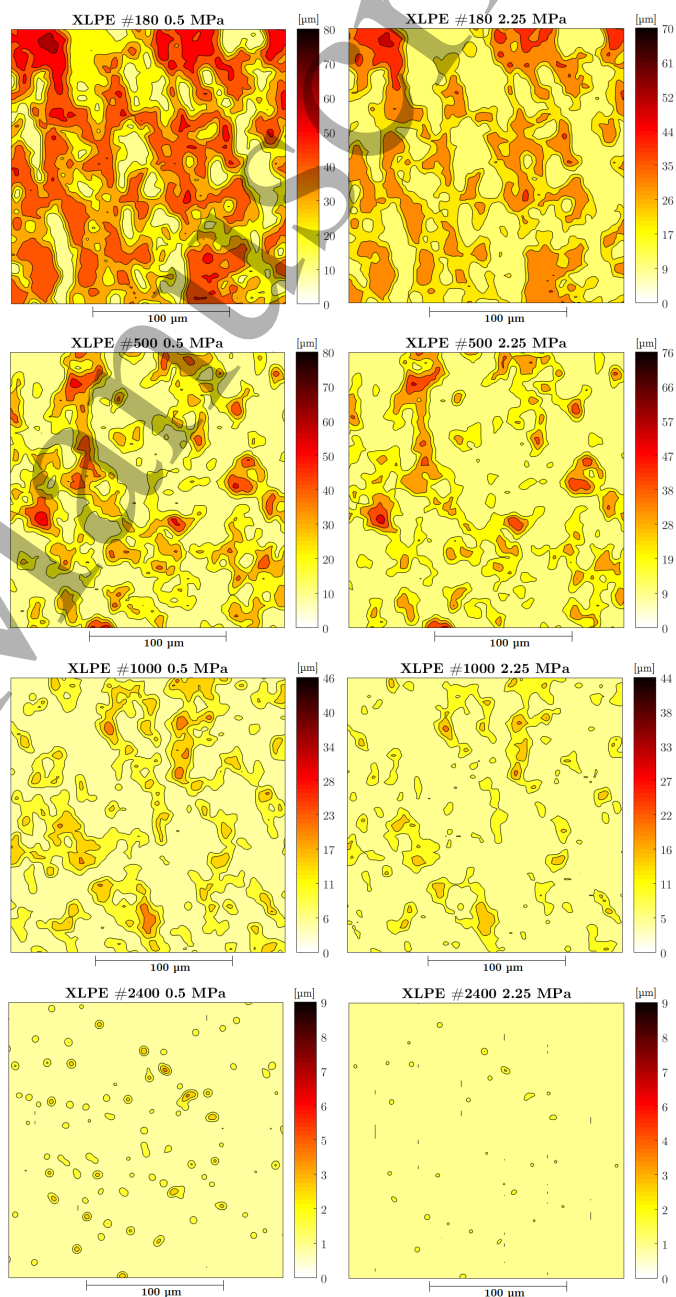

Fig. 6: Simulated XLPE–XLPE interfaces sanded using #180, #500, #1000 and #2400 at 0.5 MPa (lowest p_a) and 2.25 MPa (highest p_a) shown by filled-contour plots. In the contour plots, contact area is depicted by light yellow/white whereas cavities are represented by darker colors.
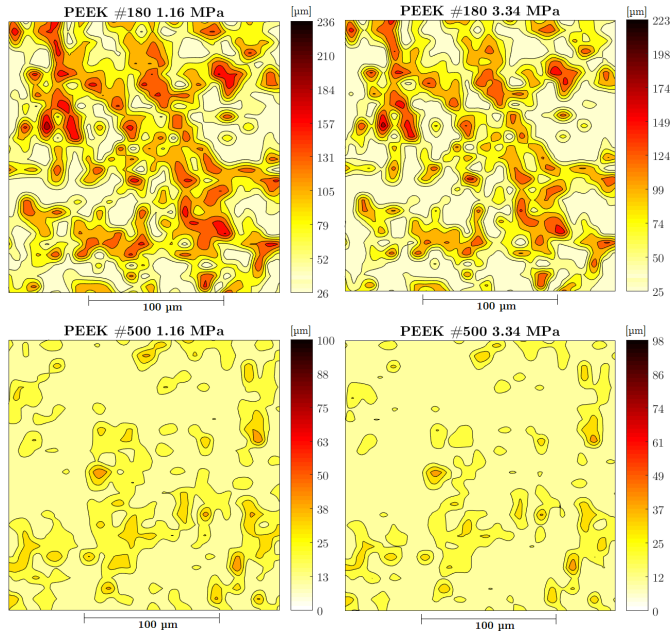
6

Fig. 7: Simulated PEEK–PEEK interfaces sanded using #180 and #500 at 1.16 MPa (lowest p_a) [29] and 3.34 MPa (highest p_a) shown by filled-contour plots.

vector in the entire mesh in the size of 1×1240 represents a 2D roughness profile similar to those presented in Fig. 8.

Considering the contour plots presented in Figs. 6 and 7, we found that the deformation of contact asperities was significantly lower in the case of PEEK (hard interface) even at higher contact pressures than in the case of XLPE (soft interface).

5.3.3. Estimated Sizes of the Largest Cavities

In this section, the sizes of the largest cavities (d_{max}), measured between two adjacent contact areas with their 90 % CIs, were estimated using the deterministic model. The purpose is to substitute d_{max} values in Eq. (8) to estimate the PDIE in the largest cavities, that will later be coupled with the submodel for the contact spot BD.

To begin with, Figs. 9(a)–(b) display the sizes of the largest cavities for the XLPE–XLPE and PEEK–PEEK interfaces with the shown roughness degrees. The authors' previous work [11], which proposed a statistical model to estimate the average sizes of cavities at solid-solid contact surfaces using 2D profiles, yielded estimated average sizes of interfacial cavities under various pressures, roughnesses, and elasticities. Fig. 9(a) indicate that the largest cavities could be 3–4 times as large as the estimated average-sized cavities in the case of XLPE, as reported in [11]. On the other hand, the sizes of the largest cavities seemed to be close to each other in the cases of PEEK and XLPE [Fig. 9(b)] despite the significant difference observed in the estimated average-sizes in [11].

6. Discussion

6.1. Sizes of the Cavities and Contact Spots

The interface simulations indicated that higher interfacial pressure led to fewer long, vented air-gaps and
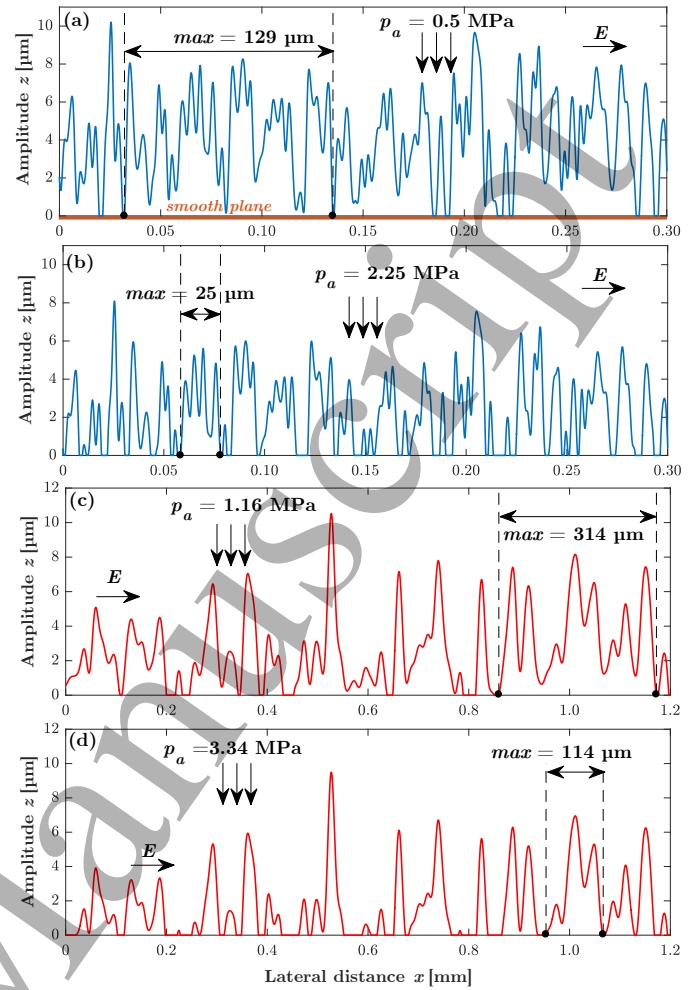

Fig. 8: Elastically deformed topography of an interface when the equivalent rough surface is pushed against the perfectly smooth plane (x-axis): (a) XLPE-XLPE #500 at 0.5 MPa. (b) XLPE-XLPE #500 at 2.25 MPa. (c) PEEK-PEEK #500 at 1.16 MPa. (d) PEEK-PEEK #500 at 3.34 MPa. E shows the direction of the tangential field component.

thus created more enclosed cavities at the interface. Likewise, the smoother the surface was, the more enclosed, smaller cavities were present. Conversely, harder interfaces brought about larger cavities, that in turn, resulted in long channels due to interconnected cavities. These findings suggest that increased contact pressure, increased elastic modulus (harder materials), and/or decreased surface roughness generate smaller cavities. Consequently, vented channels and enclosed cavities at the interface are likely to coexist, especially in the cases of moderate roughnesses, contact pressures, and material elasticities. The state of the coexistence of vented and enclosed cavities can be deemed as a transition from soft, smooth interfaces at high contact pressure to hard, rough interfaces at low pressure.

Figs. 10(a) and (c) illustrate the case when only enclosed cavities are present at an interface such as in the cases of soft materials, high contact pressure, and/or smooth surfaces. Conversely, Figs. 10(b) and (d)
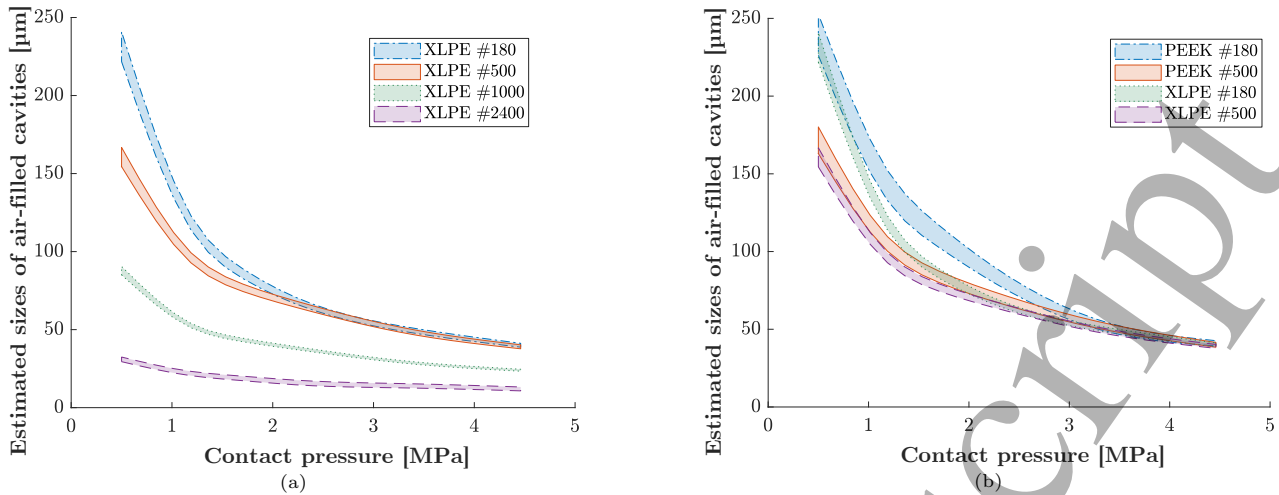
Fig. 9: The largest estimated air-gap size d_{max}: (a) XLPE–XLPE interfaces at four different surface roughnesses. (b) XLPE–XLPE and PEEK–PEEK interfaces at two different surface roughnesses.

demonstrate that, nearly, only vented channels exist at the interfaces, as observed in the cases of hard materials, rough surfaces, and/or low contact pressure. Possible surface paths likely to be tracked in the event of an interface breakdown are illustrated in Figs. 10(a)–(b) for each case. In the case of "only enclosed cavities," contact spots must be subjected to an electrical breakdown in addition to the discharge of cavities. On the other hand, in the case when air-filled, interconnected cavities are prevalent at the interface, an interface tracking path can be formed by incorporating only the vented air-gaps, as illustrated in Fig. 10(b).

6.2. Mechanisms Controlling the Interfacial Breakdown

To elucidate main mechanisms controlling the interfacial breakdown, the results of the experimental and theoretical studies are used. The results will also clarify the impacts of different sizes of cavities and contact spots on the tangential AC breakdown strength, that are covered in Section 6.1. The effect of the discharge of cavities and the breakdown of contact spots on the interfacial breakdown strength are examined separately based on the corresponding submodels introduced in Section 3 by following the sequence of mechanisms hypothesized in Section 3. It should be emphasized that the mechanisms controlling the interface breakdown are investigated for samples assembled in an optimal, dry laboratory conditions.

6.2.1. Effect of Cavity Discharge and Gas Pressure Inside of the Cavities

In this section, the correlation between the estimated cavity partial discharge field (PDIE^e) and the measured values (AC breakdown field and PDIE) is examined. It should be noted that the measured PDIE values (PDIE^m) do not necessarily characterize the inception field of the discharged cavities that had initiated an interfacial breakdown. Based on the 3D interface simulation results and the discussion in Section 6.1, interfacial tracking is likely

to be tortuous due to the presence of contact spots obstructing the propagation of streamers. The endurance of the contact spots against propagating streamers is designated using the interfacial tracking resistance of the contact spots (as introduced in Section 3), which is an insulation property of the bulk material. Moreover, cavity sizes are essential for the theoretical analysis of the interface breakdown phenomenon. However, sizes of the interfacial cavities cannot be extracted from the measured PDIE data without using an analytical model. For these reasons, the deterministic interface model was employed to determine the sizes of cavities as a function of the surface roughness, elasticity, and applied contact pressure. The estimated sizes of the cavities were then used to estimate the PDIE values. The determined cavities seem to be elongated in the electric field direction (as can be seen in Fig. 8), leading to $f \approx 1$ according to Eq. (9).

First of all, the results of the AC breakdown experiments were compared to the measured PDIE values (PDIE^m). Fig. 11(a) shows the comparison between the measured PDIE and the measured AC BDS of the XLPE–XLPE #500 interface. The difference between the 63.2 % BDS and PDIE^m (shown by the error bars) was found to be only around 10 %, implying that discharged cavities in the XLPE samples might have triggered a complete flashover in a short time. In contrast, in the case of PEEK–PEEK #500 interface [Fig. 11(a)], the mean PDIE^m values were lower than the measured mean BDS values by a factor of 1.6, suggesting that the contact spots at the PEEK interface could withstand discharges for a longer period (applied voltage was higher by 1 kV every next second). Overall, the correlation between the measured PDIE and BDS values, despite the limited number of data points, agrees with the proposed interfacial BD model that assumes that the interfacial tracking resistance is an essential electrical insulation property in the breakdown of interfaces. Therefore, the effect of the tracking resistance will be examined in the

(a) Enclosed cavities in 3D (SiR–SiR #500).

(b) Vented air-gaps in 3D (PEEK–PEEK #500).

(c) Enclosed cavities in 2D.
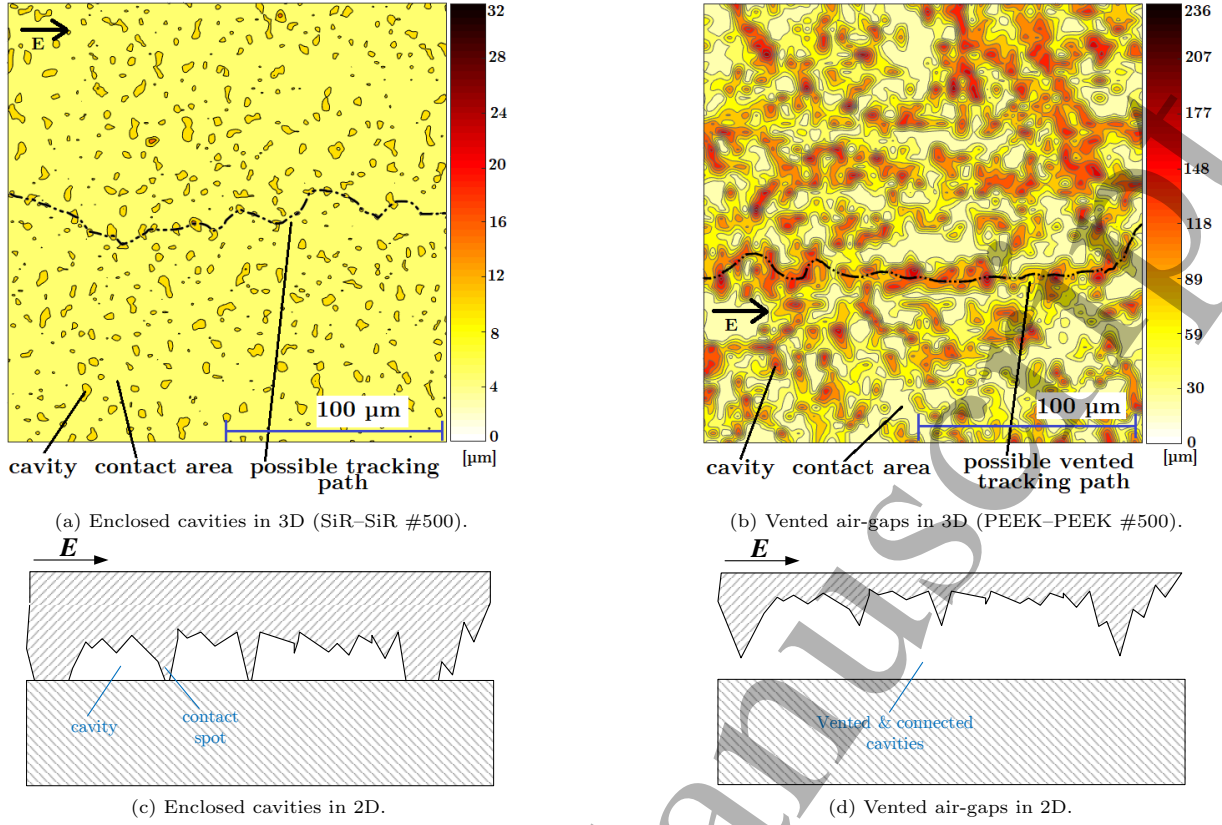

(d) Vented air-gaps in 2D.

Fig. 10: Simulated interfacial surfaces incorporating only enclosed cavities and vented air-gaps formed by interconnected cavities.

next section. Before that, the effect of the gas pressure inside of the cavities will be discussed in the following.

Using the determined largest cavity sizes (Fig. 9), estimated PDIE values are compared to the AC BDS and PDIE^m results in Fig. 11(a) under two scenarios. In addition to the results shown in Fig. 11(a), extended results are also presented in Fig. 11(b), that cover more data points at a wider pressure range from the AC breakdown experiments, performed using XLPE and PEEK with the same surface roughness (#500).[3]

In the first scenario, the pressure inside of the cavities is assumed to remain at ambient pressure because a large number of connected cavities at the interface are likely to allow the air to be squeezed out and be vented to the surroundings. However, the results of the AC breakdown experiments and the simulation results [Fig. 10(a)] indicate that the assumption of vented cavities is not entirely valid in the cases of smooth interfaces under high contact pressures and/or very soft interfaces subjected to high contact pressures. In these cases, the number of isolated cavities is very high while there are few, if not none, vented channels according to the interface simulations. Consequently, vented cavities and enclosed cavities at the interface are likely to coexist in real life.

---

[3]PD experiments were carried out only at two different contact pressures while the BD experiments were performed at four different pressures. The min./max. pressure values were determined based on initial tests [10].

The gas pressure inside of an isolated cavity may rise as a function of the change in the cavity size (the extent of which is dependent on the contact pressure and elastic modulus), which in turn, increases the discharge field strength of the cavities according to the right-side of the Paschen minimum. Thus, in the second scenario, the gas pressure inside of the enclosed cavities is estimated using ideal gas law. According to the ideal gas law, the air pressure in the enclosed cavities tends to be higher than 1 atm after the contact pressure is increased above its initial value. To model the air pressure inside of enclosed cavities, the initial gas pressure p_0—prior to the application of contact pressure—is set to 1 bar ($\approx$ 1 atm). With the increase of the applied pressure, cavities are further compressed, and hence the pressure inside of a cavity, p_c will rise according to the ideal gas law [30]:

$$p_c = \left(\frac{d_{cav_{ref}}}{d_{cav}} \right)^3 p_0 \,, \tag{11}$$

where $d_{cav_{ref}}$ is the initial cavity size in the tangential direction when p_a is equal to the reference initial applied pressure p_{ref}. Based on the right of Paschen minimum, the discharge field strength of air-filled cavities increases as a function of the gas pressure inside of the cavities.

Scenario 1: Vented cavities — $p_c = 1$ bar

The results shown in Figs. 11(a)–(b) suggest a moderate correlation between the BDS values and the PDIE^e values within the covered pressure range in the case of
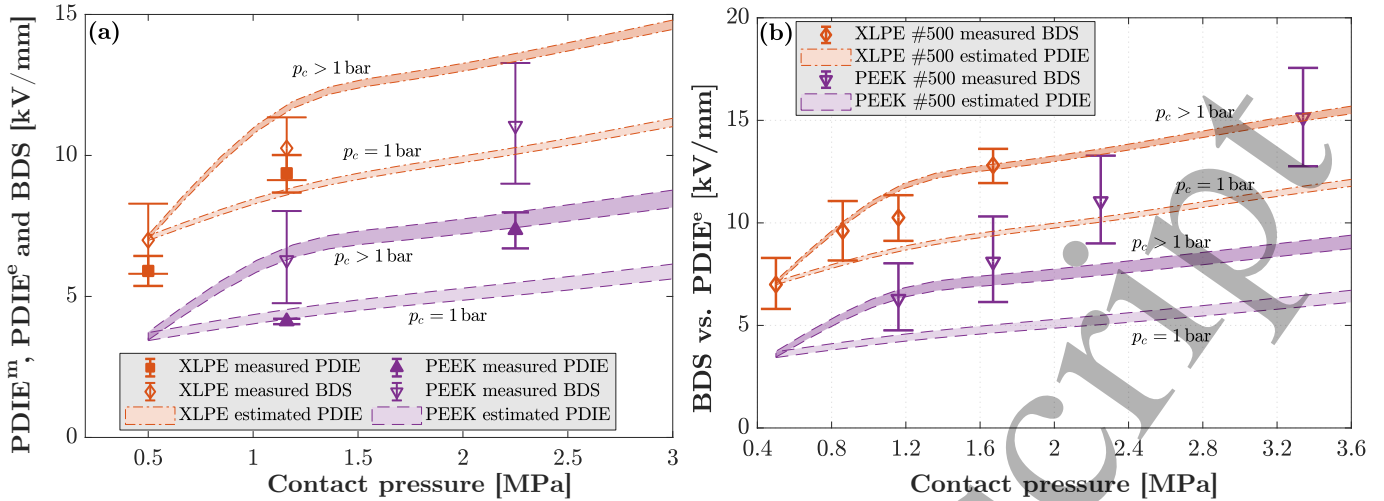
Fig. 11: Comparison of: (a) Measured PDIE ($PDIE^m$), estimated PDIE ($PDIE^e$) and measured AC BDS of XLPE–XLPE #500 and PEEK–PEEK #500 interfaces. (b) $PDIE^e$ and AC BDS of XLPE–XLPE #500 and PEEK–PEEK #500 interfaces.

XLPE–XLPE #500. The ratio of the mean BDS to the mean $PDIE^e$ ranges from 0.95 to 1.3. This deviation suggests that the interfacial breakdown is likely to be dominated by the cavity discharge between the XLPE samples at low contact pressures. Nevertheless, PEEK–PEEK #500 interfaces exhibited a relatively weak correlation between the estimated cavity discharge and the interface breakdown fields, particularly at relatively high contact pressures.

The correlation between the measured BDS and $PDIE^m$, discussed in this section, seems to be in line with the correlation between the measured BDS and $PDIE^e$ in this scenario. In the case of XLPE–XLPE #500, $PDIE^e$ values were within the confidence intervals of the $PDIE^m$ values [Fig. 11(a)]. For the PEEK–PEEK #500, on the other hand, $PDIE^e$ was comparable to $PDIE^m$ only at 1.16 MPa whereas the deviation became larger towards 2.25 MPa.

These findings hint that, in the case of higher elastic modulus, the interfacial breakdown is probably not solely governed by the discharge of vented air-filled cavities (channels), particularly at high contact pressures. There are two factors likely to cause this behavior. First, the electrical insulation properties, such as the tracking resistance, are likely to play a vital role in determining the endurance of the contact spots against breakdown. The influence of the interfacial tracking resistance of the contact spots on the interfacial breakdown will be discussed in Section 6.2.2. Second, the gas pressure inside of the enclosed cavities, whose numbers go up significantly at relatively high contact pressures as the simulation results suggested, are likely to influence the PDIE of the cavities.

The effect of the gas pressure is discernible in the cases of relatively soft interfaces. For instance, the $PDIE^e$ values of the XLPE interfaces between very rough (#180) and very smooth (#2400) sample surfaces are shown in Fig. 12. The correlation between the $PDIE^e$ and the measured AC BDS values was moderate at relatively low contact pres-

sures while it became weaker toward higher contact pressures. The increased deviation between the $PDIE^e$ and the BDS values was probably due to d_{max} values becoming significantly lower [Fig. 9(a)] and the notable increase in the number of the enclosed cavities as compared to vented channels. Identical trends were also observed for the SiR–SiR #500 interface (Fig. 13) in the case of $p_c = 1$ bar. These observations support the simulation results such that increased contact pressure, particularly in the cases of relatively soft and/or smooth interfaces, leads to more and smaller enclosed cavities where the impact of the gas pressure inside of cavities becomes more prominent.

Fig. 12: Comparison of $PDIE^e$ and AC BDS of XLPE–XLPE #180 and XLPE–XLPE #2400 interfaces: (i) Vented cavity scenario ($p_c = 1$ bar). (ii) Unvented cavity scenario ($p_c > 1$ bar).

Scenario 2: Enclosed (unvented) cavities — $p_c > 1$ bar

Using Eq. (11), the gas pressure values inside of the cavities, p_c were estimated based on the change in the cavity size, and they were substituted into Eqs. (8)–(10) to calculate $PDIE^e$.

As presented in Fig. 6, the increased contact pressure
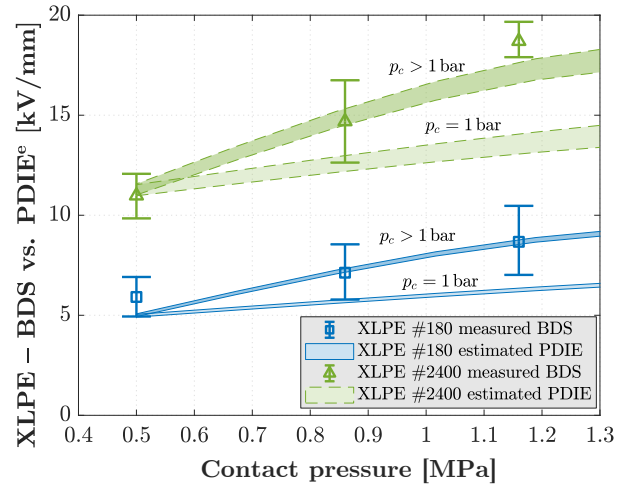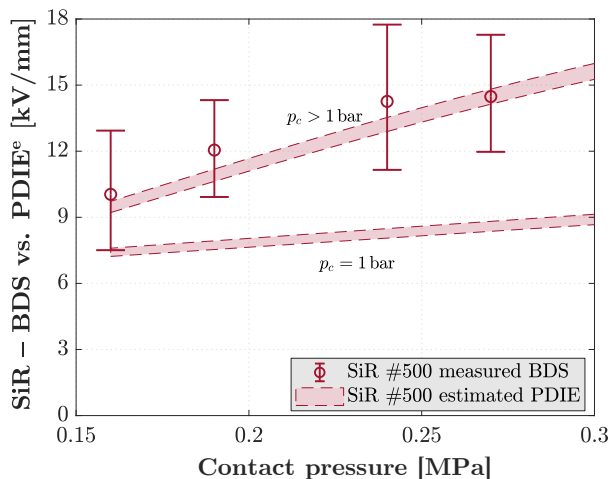
Fig. 13: Comparison of PDIE^e and AC BDS of SiR–SiR #500 interfaces: (i) Vented cavity scenario ($p_c = 1$ bar). (ii) Unvented cavity scenario ($p_c > 1$ bar).

in the case of the smoothest interface, XLPE #2400, led to an almost perfect/ideal contact between the XLPE samples. In conjunction with the larger contact area that the simulations suggested, very high AC BDSs were recorded in the case of XLPE #2400, particularly at higher contact pressures, as displayed in Fig. 12. In addition, the measured 63.2 % BDS at 0.5 MPa in the case of XLPE #180 became 1.4 times the measured 63.2 % BDS at 1.16 MPa. For the smoothest interface (#2400), the rise in the BDS versus pressure increase was more significant by a factor of 1.7. These findings suggest that smoother interfaces respond to increased contact pressure to a larger extent, leading to a higher BDS. Similarly, the simulated SiR–SiR #500 interface at 0.16 MPa (highest contact pressure value applied in the experiments determined by initial tests), as shown in Fig. 10(a), indicates that there were many enclosed cavities even at very low pressure, which were broken into even smaller cavities at a slightly higher contact pressure (0.27 MPa). The very high AC BDS values of SiR–SiR #500 displayed in Fig. 13 suggest that there were probably numerous enclosed cavities even at a relatively low contact pressure, where the gas pressure was probably greater than 1 bar.

The trends observed in the cases of XLPE–XLPE and SiR–SiR interfaces are likely to stem from the reduced cavity sizes and the increased gas pressure in those cavities. The estimated PDIE values in the case of $p_c > 1$ bar (see Figs. 12–13) correlated highly with the measured BDS values. Based on this high interdependence, it can be inferred that the increased gas pressure inside of enclosed cavities was likely to have contributed to the very high BDS values achieved at smoother and/or softer interfaces, especially at high contact pressures in the AC breakdown experiments.

On the other hand, although the estimated d_{max} sizes of the XLPE and PEEK are comparable in the given contact pressure range [Fig. 9(b)], the degree of correlation

between the PDIE^e and the BDS values for $p_c > 1$ bar [Fig. 11(b)] are different for XLPE and PEEK interfaces. Considering the trends observed in Figs. 11–13 and the discussion on the BD mechanisms so far, it is fair to infer that the interfacial breakdown in the case of higher elastic modulus (EPOXY–EPOXY[4] and PEEK–PEEK) is not solely governed by the discharge of air-filled cavities/channels. In the next section, the influence of the contact spots is finally examined.

6.2.2. Effect of Contact Spots

The estimated local field enhancements at the contact spots, E_{cnt}, are compared with the estimated PD resistances, E_{tr}, of the XLPE, EPOXY, and PEEK (of #500 roughness for all) in Fig. 14 compares. Based on the definitions in Fig. 4, *instant I* points out the inception of discharge in the largest cavities, whereas *instant II* indicates the contact spots succumbing to the intense local fields and break down. Based on the proposed model described in Appendix B, we estimated E_{cnt} and E_{tr} values using Eqs. (B.1)–(B.3). E_{app} values used for the *instant I* were the estimated PDIE valuess [Eq. (10)] while the measured 63.2 % BDS values were used for the *instant II*.

The estimated E_{cnt} and E_{tr} values are displayed in Fig. 14 at both instants. Fig. 14(a) indicates that once the cavities are discharged, the XLPE is not likely to endure the enhanced local fields due to the low estimated tracking resistance, and this will probably lead to an interfacial breakdown. This finding clearly supports the relatively high correlation between the measured BDS and PDIE (both measured and estimated) in the case of XLPE (see Fig. 11). Discharged cavities at the XLPE–XLPE interfaces probably evolved to a complete flashover in a short time because the contact spots were less likely to withstand the enhanced fields for a longer period due to the relatively low estimated interfacial tracking resistance of the XLPE. Conversely, the estimated enhanced local fields may not be sufficiently high to exceed the interfacial tracking resistance in the cases of hard interfaces such as EPOXY–EPOXY and PEEK–PEEK at the *instant I*. For instance, the relatively weak correlation between the measured BDS and PDIE (both measured and estimated) for the PEEK–PEEK #500 indicate that although cavities were discharged, contact spots with high estimated tracking resistance at the PEEK interface seems to have withstood the intense local fields longer than the XLPE interface lasted. For all of the interfaces, the estimated E_{cnt} values at the *instant II* clearly indicate that the local fields surpassed the tracking resistances of the materials.

In the cases of the smoothest and roughest XLPE interfaces, when discharge activity started in the largest cavities, the estimated enhanced fields were close to the estimated interfacial tracking resistance of the XLPE, as pre-

---

[4]The measured BDS and the estimated PDIE values of EPOXY-EPOXY interface are quite similar to those of PEEK–PEEK, so the results of the PEEK–PEEK were selected to represent the hardest interface.
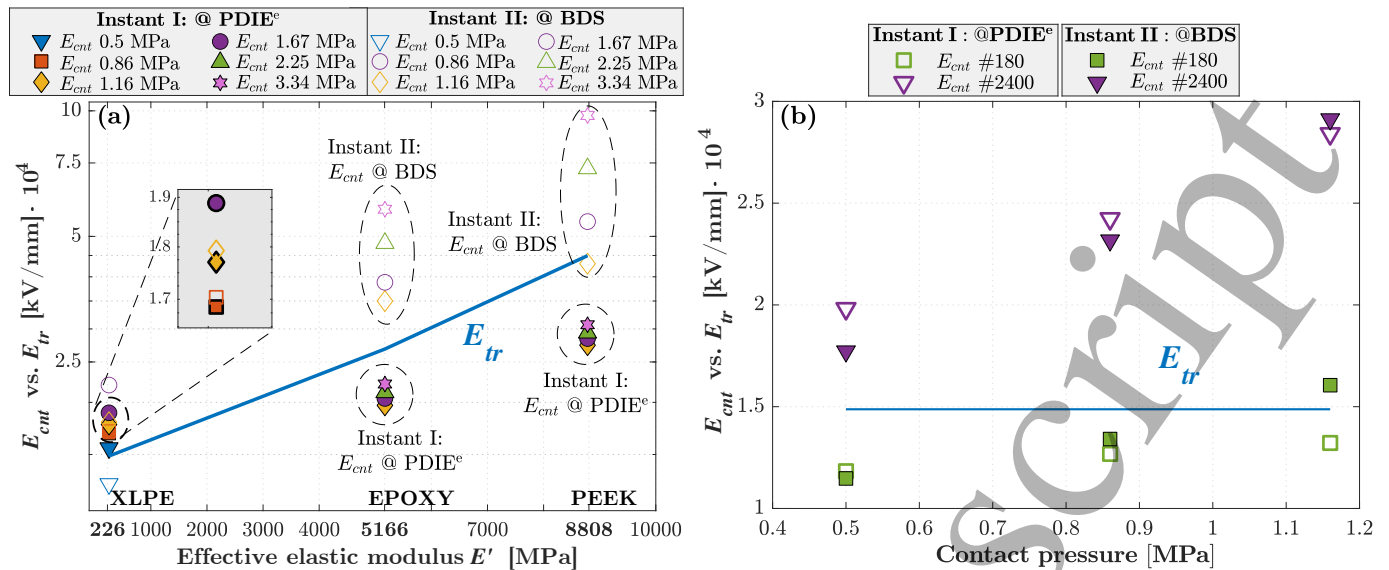
Fig. 14: Estimated enhanced fields E_{cnt} vs. tracking resistance E_{tr} at $p_a = 0.5 - 3.34$ MPa at the instants of cavity discharge and breakdown of contact spots: (a) XLPE #500, EPOXY #500, and PEEK #500 interfaces. (b) XLPE–XLPE interfaces at two different surface roughnesses. Instants I and II represent the moments when PD and BD occur, respectively, as denoted in Fig. 4 ($G = 7000$ J/m^2 and $r = 1.2$ µm for the XLPE; $G = 13000$ J/m^2 and $r = 1.2$ µm for the EPOXY; and $G = 20000$ J/m^2 and $r = 1.2$ µm for the PEEK [20, 31]).

sented in Fig. 14(b). At smoother interfaces, the estimated enhanced field values appeared to be sufficiently intense to result in the breakdown of the contact spots. The magnitudes of the estimated local fields did not significantly increase from the PD inception until interface breakdown [from *instants I to II* in Fig. 14(b)] because the estimated PDIE values were close to the measured BDS values. Consequently, Fig. 14(b) highlights again that once the cavities were discharged, the low (estimated) interfacial tracking resistance of the XLPE was not likely to withstand the enhanced local fields long enough to prevent an interfacial breakdown from occurring in a short time. Also, the increased contact pressure resulted in lower d_{max}, and hence relatively high PDIE^e values, leading to relatively high E_{cnt} values based on Eq. (B.1). These findings corroborate the hypothesis that the effect of the interfacial tracking resistance on the interfacial breakdown is not insignificant. In particular, its influence has been found to be more prominent at higher contact pressures, harder interfaces, and/or smoother surfaces.

These findings also strongly agree with the relevant studies in the literature. Kato et al. [8] reported that streamer propagation was inhibited at an interfacial region where the pressure was relatively high (supporting the presence of enclosed gaps), which led to a higher AC BD voltage, while the lowest AC BD voltage was measured in the case of the hardest interface. Du et al. [27, 32] also focused on the PD-initiated light emission due to the recombination of charged particles with opposite polarities and energetic particle bombardment to explain the mechanisms accountable for the local breakdown of contact area. They stated that the energetic particle bombardment is likely to disrupt the covalent bonds that hold the polymer together [27]. The light emission also gives rise to the ac-

celeration of the chain scission [27]. The bombardment of particles is likely to cause the loss of part of their energies, and trapped carriers (electron or hole) arise at the interfacial contact areas [27]. As a result, low-density regions at the interface are formed, that are more likely to undergo electrical breakdown under AC excitation [33]. For this reason, a discharge channel usually follows a tortuous path with lower PD resistance (i.e., low-density regions). Once the contact surface between two cavities is broken-down, the discharged cavities are bridged, resulting in a larger discharge channel. As concluded by Gao et al. [27], the degradation and the breakdown of the local contact area are essential for the discharge channel to propagate at the interface.

Interface surfaces, inspected using a digital microscope after the experiments, provide supporting evidence for the effect of contact spots on the interfacial breakdown. Fig. 15(a) displays the surface of an XLPE sample that underwent an interface breakdown. The encircled area at the surface indicates interfacial microtracking activity near the top electrode, but the propagation of the streamers was most likely hindered due to the contact spots on their way. The interface tracking path shown by the arrows might be one such streamer that could propagate owing to connected cavities or by breaking down the contact spots obstructing it. The surface of a PEEK sample, subjected to an interfacial breakdown, provides more explicit evidence, as shown in Fig. 15(b). The enclosed area unveils an interfacial microtrack (erosion/carbon decomposition in microcracks of insulation) of a length of about 0.24 mm. The tracking path is located near the main breakdown track, but neither of its ends is connected with other tracking paths. Thus, it is an isolated microtrack, which possibly bridged two contact

areas but was stopped by the high tracking resistance of the contact spots at PEEK. The images suggest that there were discharge activities in several cavities/channels that could not evolve to a complete flashover (a dedicated study to monitor this phenomenon can be found in [29]).
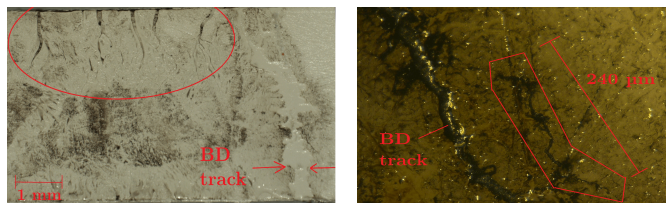
(a) XLPE–XLPE #500 1.16 MPa.   (b) PEEK–PEEK #500 1.16 MPa.

Fig. 15: Microtracking observed at interfaces between broken-down samples. The widths of the microtracks range from 4 to 8 μm.

7. Conclusion

In this paper, the correlation between the tangential AC BDS of solid-solid interfaces and the interface morphology was studied theoretically and experimentally. An extensive interface breakdown model was proposed to explore the effect of different interfacial breakdown mechanisms. The backbone of the breakdown model is a deterministic contact model built around the tribology of solid surfaces. It was used to determine the sizes of the interfacial cavities and to simulate the 3D deformation of the surface protrusions based on the surface roughness, contact pressure, elastic modulus, and hardness of an interface. The estimated sizes of cavities and contact areas were then coupled with a thorough breakdown model that addressed cavity discharge and breakdown of contact areas, separately.

The interface contact model indicated that increased contact pressure reduced the number of long, vented air-gaps, and thus, created more enclosed cavities at an interface. Likewise, the smoother the interface was, the more enclosed, smaller cavities were present. Conversely, harder interfaces brought about larger cavities, and thus, long vented air-gaps were formed by the interconnected cavities: vented and enclosed cavities at an interface coexist in real life. Thus, the gas pressure inside of the enclosed cavities tends to rise as a function of the change in the cavity sizes, the extent of which is dependent on the contact pressure and elastic modulus.

The results of the AC breakdown and PD experiments indicated that interface pressure, roughness, and elastic modulus significantly affected the BDS of solid-solid interfaces. The interfacial BDS values in the cases of softer interfaces, SiR–SiR and XLPE–XLPE, were found to be up to 58 % higher than those of the harder interfaces, EPOXY–EPOXY and PEEK–PEEK at the same contact pressure. Likewise, smoother interfaces and higher contact pressures led to considerably higher AC BDS values (up to 20 kV/mm). The increased gas pressure inside of enclosed cavities was likely to have contributed to the very high BDS values achieved at smoother and/or softer interfaces,

especially at high contact pressures in the AC breakdown experiments.

The interfacial breakdown in the case of XLPE–XLPE has been found to be strongly dominated by the discharged cavities due to the relatively low estimated interfacial tracking resistance of XLPE. In other words, discharged cavities have resulted in an interfacial failure more easily because the contact spots could not withstand the enhanced fields for a long time. In addition, different surface roughnesses in the case of XLPE–XLPE interfaces have also suggested a clear correlation between the cavity discharge and the interface breakdown in the cases of rough and smooth surfaces. On the other hand, in the case of hard interfaces with higher elastic modulus such as PEEK–PEEK, contact spots may have endured the local enhanced fields longer due to the relatively high estimated tracking resistance of PEEK. To sum up, the results have suggested that the influence of the interfacial tracking resistance of contact spots on the interface breakdown becomes more prominent at higher contact pressures, interfaces between harder materials and/or smoother surfaces.

To our knowledge, the proposed interface breakdown model is novel in incorporating diverse interdisciplinary fields. As a result of the clear agreement between the theoretical results and experimental results, we believe that the model deserves further attention.

Acknowledgment

APPENDICES

Appendix A. Deterministic Contact Model

A.1. Implementation of the Variational Principle

Rough surfaces can be digitized and simulated without any further assumptions for the diffusion and density of rough asperities using "the variational principle" [2, 12, 13]. It employs a direct, quadratic numerical programming method that returns a unique solution for rough surface contact problems, where the computation time is substantially shorter compared to the conventional matrix inversion technique because there is no additional iteration process involved in the variational approach [13]. Hence, converging solutions for the contact problems of 3D rough surfaces with multiple contact points becomes viable.

Solving a variational problem is identical to finding the minimum value of an integral equation that can be approximated to a "boundary value problem" of differential equations for a mechanical system [2]. Two minimum energy principles, namely "total elastic strain energy" and "total complementary potential energy", can be employed for solving mechanical problems in the variational approach [2, 13]. In the cases where the real area of contact and the pressure distribution are uncertain, the minimum "total complementary potential energy principle" for rough

surface contacts requires the lowest complementary energy value of the contact surface system, realized using the minimum value of an integral equation.

The contact between real-life topographies leads to plastic deformations at the contact spots, even under relatively light loads [12]. For instance, Tian and Bhushan [13] constructed their proposed model on the variational approach for both elastic and elasto-plastic materials, allowing computation of the resulting plastically deformed surfaces. The variational principle simplifies the problem to a "quadratic mathematical programming problem" owing to an "infinite-to-finite dimension transformation" [2]. The variables in the variational method, namely, the real contact area and the contact pressure distribution, are used to find the minimum value of the "total complementary potential energy" [2, 13].

A.2. Discretization of Surface Profiles

An approximate value for the "minimum complementary potential energy" is acquired by discretizing the entire interfacial contact surface (obtained using the optical profilometer), i.e., the computational domain represented by Ω in Eqs. (1)–(3) into a mesh of smaller discrete elements [13], as illustrated in Fig. A.1. Thereby, the surface deformation (cavities and contact spots) is associated with the applied contact pressure.

The obtained 3D surface profile of each specimen is stored in a 480×640 mesh. The assessment length of each row vector of the measured profile is discretized into 10240 elements, resulting in an equivalent, discrete mesh with a size of 480×10240 (see Fig. A.1). The measured profile by the profilometer spans a lateral length of L, which is a fragment of the thickness of the sample T. The total applied load W_m is thus scaled by L/T as described in [34]. The samples studied are of $L_x = 1.25$ mm, $L_y = 0.94$ mm, and $T = 4$ mm.

The correlation between contact pressure and elastic deflection is defined by Eq. (3), and, by the application of
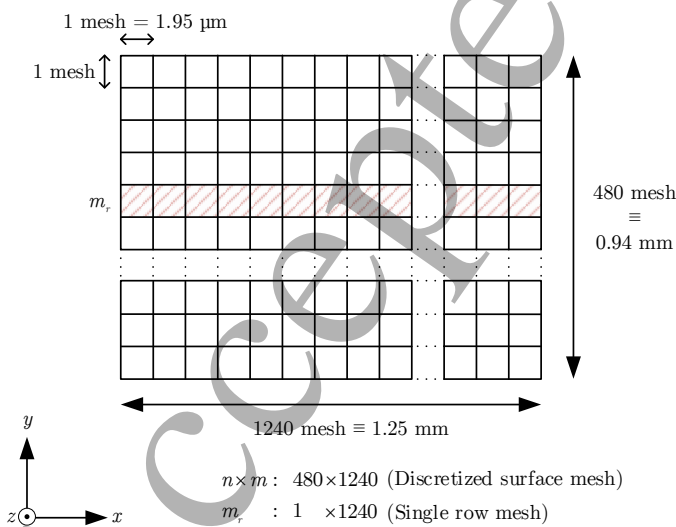
a finite difference method (FDM), it is discretized into:

$$\delta_{ei} = \sum_j^M K_{ij}\, p_j\,, \qquad (A.1)$$

where M represents the total number of initial contact spots, K_{ij} is the arbitrary discretization of K, and p_j is the discretized contact pressure in each cell of the mesh.

The equation defining the total potential complementary energy, F is in a quadratic form, due to the correlation between the elastic deflection and the contact pressure:

$$F_i = \frac{1}{2} \sum_i^M p_i \sum_j^M K_{ij}\, p_j - \sum_i^M p_i \left(h_{2i} - h_{1i} - \delta_{p_i} \right), (A.2)$$

which can be reformulated in a matrix form [12], viz:

$$F = \frac{1}{2}\, \mathbf{p}\,\mathbf{K}\,\mathbf{p} - \mathbf{p}\,(\mathbf{h_2} - \mathbf{h_1} - \boldsymbol{\delta_p})\,. \qquad (A.3)$$

A pressure p value must be determined that yields the zero gradient of F, i.e., $\nabla F = 0$ to find a minimum energy value satisfying F. The gradient $\nabla \triangleq \partial/\partial\,\mathbf{p}$ of F in respect of p is given by [12]:

$$\begin{aligned} \nabla F &= \mathbf{K}\,\mathbf{p} + \boldsymbol{\delta_p} - (\mathbf{h_2} - \mathbf{h_1}) \\ &= \boldsymbol{\delta_e} + \boldsymbol{\delta_p} - (\mathbf{h_2} - \mathbf{h_1})\,. \end{aligned} \qquad (A.4)$$

A.3. Solution Technique

The solution method proposed in this section minimizes F using a nested iterative process by finding a p that leads to $\nabla F = 0$ [12]. The force-balance condition is controlled by an inner loop in the iterative process, and an outer loop carries on iterating until all contact points dwell adequately close to the contact plane [12]. When the inner loop is complete, based upon the position of the contact points and the pressure component, an "influence matrix" is built to correlate the contact pressure to the displacement of the surface profile [2]. Following this, "the minimum total complementary potential energy" incorporating the information of the displacement and pressure is acquired by employing "a direct quadratic mathematical programming technique" [13]. Since forces in the opposite course to the movement of interfacial surfaces in contact are not permitted, $p_j \geq 0$ where $j = 1,...,M$ limits the quest for a minimum value of Eq. (A.2). It should be highlighted that the number of the ultimate contact spots satisfying the limit, $p_j \geq 0$, is likely to be lower than M. Overall, this solution technique is reported to be very robust as the algorithm never diverged [2, 12].

In the computer program running the algorithm, initially, 3D surface profiles of the two surfaces forming the interface are imported. Subsequently, the "equivalent rough contact surface" (sum surface) is generated. Next, the contact surface is discretized into mesh components, representing the protrusions/asperities. Then, an iteration loop is executed to compute elastic deformation. In

Fig. A.1: Scanned surface data discretized into a mesh of 480×1240.

1 mesh = 1.95 μm

1 mesh

m_r

480 mesh ≡ 0.94 mm

1240 mesh ≡ 1.25 mm

$n \times m$: 480×1240 (Discretized surface mesh)
m_r : 1 ×1240 (Single row mesh)

case the pressure at any contact spots goes beyond the material hardness (main constraint of the algorithm, as mentioned at the beginning of the section), a fraction of the surface at that specific vertex is discarded, and then the contact spot is classified as plastic. A new elastic solution is then attained based upon the altered profile containing plastically deformed spots. In case the pressure at plastic contacts does not reach a predefined level, the plastic deformation at those specific points must partly be eliminated [12]. The iterations continue by incrementing the applied load until a force-balance is achieved, i.e., until the pressure at all plastic points dwells within/between the predefined lowest level and the hardness of the softer material at the corresponding applied load [12]. The analysis is run for contact points where pressure is greater than zero, $p_j > 0$. The iterations continue until $\delta_{\mathbf{e}}$, $\delta_{\mathbf{p}}$, and $\mathbf{p}$ satisfy Eq. (A.4).

The elimination of the extra iteration cycles due to the "conventional matrix inversion" methods leads to a significantly accelerated iteration cycle and can be deemed the main advantage of this algorithm [13].

A.4. Computation of Real Area of Contact

The number of discretized elements that have a pressure value higher than zero (N_{cnt}) is given by:

$$N_{cnt} = \frac{1}{n_i} \sum_{i=1}^{n_i} \sum_{j=1}^{n_j} \left| \operatorname{sgn}(p_{ij}) \right|, \qquad (A.5)$$

where sgn represents the signum function that extracts the sign of the contact pressure. In the deterministic model, the contact pressure is zero at the asperity peaks, whereas it is a nonzero positive real number at the contacting points, represented as:

$$\operatorname{sgn}(p_{ij}) = \begin{cases} 1 & \text{if } p_{ij} > 0, \\ 0 & \text{if } p_{ij} \leq 0. \end{cases} \qquad (A.6)$$

Based on Eq. (A.6), $\left| \operatorname{sgn}(p_{ij}) \right|$ in Eq. (A.5) reduces to sgn (p_{ij}). The number of discrete elements, N_d, is then given by $N_d = n_i \times n_j$. The ratio of the total contact area to the nominal area $A_{re,d}/A_a$ can be calculated as a fraction of the number of discretized elements N_d:

$$A_{re,d}/A_a (\%) = \frac{N_{cnt}}{N_d} \times 100, \qquad (A.7)$$

where the subscript d in $A_{re,d}$ represents the estimated real contact area in the discrete environment of the deterministic model to differentiate it from the A_{re} in the statistical model. As mentioned in Appendix A.2, the discretized surface data are stored in a 480×10240 matrix, where $n_i = 480$ and $n_j = 10240$.

Appendix B. Estimation of the Breakdown Strength of Contact Spots

In this section, the BDS of contact spots is modeled. The model incorporates two empirical submodels to estimate the enhanced local fields at the edges of the discharged cavities (at the contact spots) and the interfacial tracking resistance of the contact spots, respectively.

B.1. Estimation of Enhanced Fields at the Contact Area

Although the applied electric field is uniform, strong non-homogeneous local fields arise at the contact spots that enclose the discharged cavities [18], as we also confirmed it using finite element method, as shown in Fig. B.1. The field strength in a discharged cavity significantly drops due to the high electrical conductivity of the discharge spark. Until the discharge is quenched, the contact spots undergo an increased electric field, as depicted in Fig. B.1, due to the increased voltage at the contact area. However, the enhanced fields may not be sufficiently high to induce a breakdown on the contact area [27]. The interfacial tracking/PD resistance of the insulation substantially determines whether the resulting intense local fields can trigger a complete interfacial flashover [19–21].
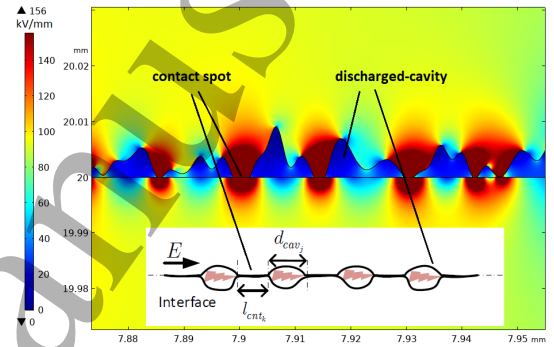

Fig. B.1: Electric field distribution at the XLPE–XLPE #180 interface in the case of discharged cavities (representing the duration between *instants* I and II in Fig. 4) performed using finite element method (equivalent rough surface data, as illustrated in Fig. 2, was exported to COMSOL Multiphysics).

It was shown that the locally enhanced fields at the contact spots can accurately be emulated by a needle-plane (point-plane) or a needle-needle electrode arrangements [19–21]. Empirical models were also widely proposed to estimate the peak electric field for the point-point or point-plane configurations [20, 21, 35]. Combining these two approaches, the endurance of the contact spots against the locally strong fields is modeled in this section.

When a dielectric between two electrodes, where either (or both) electrode has a sharp conductive section, is subjected to rated/average field strength, the electric field at the sharp section is enhanced significantly [21]. The enhanced field can be equal to or greater (by several orders of magnitude) than "the estimated intrinsic breakdown strength" of dielectric materials [21, 23]. The increased local field on the contact area is approximated using a point-point electrode arrangement:

$$E_{cnt} = \frac{V_{app} \sqrt{1 + r_n/l}}{r_n \operatorname{arctanh}\left[\frac{1}{\sqrt{1 + r_n/l}} \right]}, \qquad (B.1)$$

where r_n is the radius of the tip of needle (usually with a tip radius of $0.1 - 0.3 \, \mu\text{m}$), V_{app} is the applied voltage, l is

the thickness of the bulk polymer between the electrodes [21]. To calculate V_{app}, the applied field E_{app} is multiplied by the nominal thickness of the interface, d_{int}, since the applied field is homogeneous (Rogowski electrodes). In addition, to compute the thickness of the bulk insulation between the electrodes, l, the total length of the contact spots, i.e., the effective interface length (l_{eff}) is required to be substituted for l in Eq. (B.1). Based on the contact model shown in Fig. 3, l_{eff} is calculated by the summation of the length of each contact spot:

$$l_{eff} = \sum_{k=1}^{m_r} l_{cnt_k} \equiv d_{int} - \sum_{j=1}^{n_r} d_{cav_j}, \qquad (B.2)$$

where m_r is the total number of contact spots in a single row vector/mesh, as illustrated in Fig. A.1. (n_r is total number of cavities.)

B.2. Estimation of Interfacial Tracking Resistance of Contact Spots

Interfacial tracking/PD resistance of insulation materials have been investigated thoroughly using needle-needle or needle-plane electrodes excited with AC, DC or impulse [19–21, 23, 33, 35]. Based on the empirical study done in [20], the tracking resistance E_{tr} was modeled as:

$$E_{tr} = \left(\frac{16\, G\, E'}{\varepsilon_0{}^2\, \varepsilon_r{}^2\, r} \right)^{1/4}, \qquad (B.3)$$

where G is the toughness $[\mathrm{J/m^2}]$, E' is elastic modulus [Pa], ε_0 is the permittivity of vacuum [F/m], ε_r is the dielectric permittivity [F/m], and r is the radius of the primary "tubular branch of the breakdown channel" (interface tracking path) [m] [20, 23].

The PD tracking is a momentary breakdown mechanism, not an aging mechanism. Based on the empirical results, the duration from the initiation of interfacial tracking to breakdown is estimated to be $\lesssim 10^{-7}$ s [20, 23]. For this reason, time is not a parameter in Eq. (B.3). Breakdown streamers can be initiated by various agents and sources; such as a microcavity, an impurity/foreign particle, an electrode non-uniformity, an electrical tree, or a non-uniform property of the dielectric [20]. The radius r is determined based on the cause of the flashover. Since the source is emulated by the sharp needle tip in this approximation, the radius of the interface tracking path is assumed to be the same as that of the needle tip ($r = r_n$).

Appendix C. Details on the Methodology

The electrical and mechanical properties of each material is shown in Table C.1. It also incorporates the calculated effective modulus of each interface formed between the same materials using Eq. (5).

In the experiments, the test setup was placed in an oil-filled container (Midel 7131) to ward off external flashovers. The force of the electrodes against the samples were adjusted using a helical spring to ensure two electrodes does not carry any shear load. To that end, firstly,

the spring length was fine-tuned using a pressure sensor. Secondly, the samples were assembled in dry conditions and then the load was exerted. Subsequently, while the load was in position, the spring was retracted and released back to remove any residual shear load. Finally, the container was filled with the oil to inhibit oil migration to the interface. Mechanical loads ranging from 3 to 75 kg $(0.16-3.34$ MPa) were used to push down the top sample (vertically) to the bottom sample at the desired contact pressures, as exhibited in Fig. C.1. The mean interfacial pressure was then determined using the nominal contact area of $A_a = 4\,\mathrm{mm} \times 55\,\mathrm{mm} = 220\,\mathrm{mm^2}$. The lowest and highest pressure levels were determined in initial tests by inspecting the interfaces against oil penetration and excessive deformation. Sealing grease was applied around the interface to minimize the likelihood of oil penetration. For example, testing of the XLPE–XLPE interface was not viable at pressures higher than 1.67 MPa because of the excessive deformation of the specimens. Similarly, the SiR samples started to deform above 0.27 MPa, rendering the testing at higher contact pressures not possible due to the likelihood of oil penetration. Oil-mate interfaces had also been tested to verify the reliability of the setup in preventing undesired oil penetration within the determined contact pressure range for each interface [7]. Each test took between $20-80$ s, so the samples were submerged in oil no longer than a few minutes; thus the percolation/permeation of oil was not at stake.
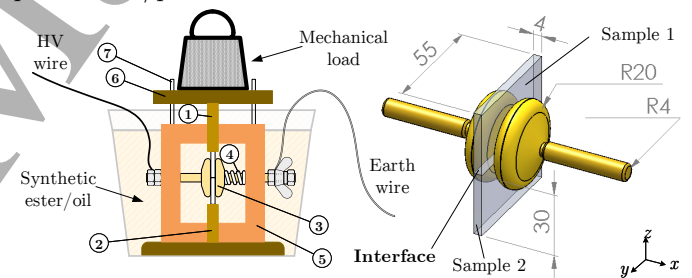

Fig. C.1: The test setup used in the AC breakdown experiments: (1) Top pressure conveyance block (adjustable). (2) Bottom pressure conveyance block (fixed). (3) Rogowski-profile electrodes. (4) Helical spring. (5) Supporting frame. (6) Epoxy plate. (7) Load stabilizers (epoxy). Dimensions are given in mm. For details, refer to [6].

For the AC breakdown tests, we subjected all samples with a homogeneous AC electric field using a 50-Hz AC ramp voltage at the rate of 1 kV/s until breakdown. We carried out eight measurements using an unused pair of specimens for each of eight repetitions to test each interface at each surface roughness and contact pressure. The same type of AC voltage ramp of 1 kV/s was applied in the PD tests. When the PD activity started, the voltage was maintained for 2 minutes at the inception voltage PDIV, and the PD data was recorded. Following this, the voltage was reduced to zero, and a five-minute interval was given before repeating the procedure. Four virgin pairs of samples were used in each experiment, and each pair was tested three times with five-minute breaks in between. Hence, 12 measurements in total were recorded for each set

Table C.1: The electrical and mechanical properties of each material used for the models and simulations.

Polymer	Elastic modulus ξ [MPa]	Poisson's ratio v	Hardness H [MPa]	Relative permittivity ϵ_r	Interface	Effective Modulus E' [MPa]	Interface type
SiR	59	0.48	2.2	2.8	SiR−SiR	109	Very soft
XLPE	200	0.46	11.2	2.3	XLPE−XLPE	226	Soft
EPOXY	4425	0.38	12.3	4.6	EPOXY−EPOXY	5166	Hard
PEEK	7515	0.38	12.4	2.8	PEEK−PEEK	8808	Very hard

of PD tests. Interested readers can refer to [6, 10] for the details of the experimental setup (for AC breakdown and PD tests) and the experimental procedure.

Two-parameter Weibull distribution was used to statistically assess the breakdown and PD data. The characteristic value of the Weibull, 63.2 %, with the 90 % confidence intervals (CI) were used. In each case, goodness-of-fit for the Weibull regression lines was checked using the guidelines in [36]. Lastly, to provide the deterministic model with the real 3D surface data, we scanned/characterized the morphology of the polished sample surfaces using a 3D-optical profilometer (Bruker ContourGT-K). 50X magnification (sampling resolution: 0.2 µm lateral and 3 nm vertical) was chosen to scan a surface area of 1.25 mm × 0.94 mm, data of which is stored in a 480 × 640 mesh.

References

[1] J. Greenwood, J. Tripp, The contact of two nominally flat rough surfaces, Proc. Instit. Mech. Eng. 185 (1) (1970) 625–633.

[2] B. Bhushan, Contact mechanics of rough surfaces in tribology: multiple asperity contact, Tribology Letters 4 (1) (1998) 1–35.

[3] Y. P. Zhao, L. S. Wang, T. X. Yu, Mechanics of adhesion in MEMS—a review, Journal of Adhesion Science and Technology 17 (4) (2003) 519–546.

[4] B. Zhu, Z. Jia, H. Hu, X. Ouyang, X. Wang, Relationship between the Interfacial Ramped DC Breakdown Voltage and the Morphology of the XLPE/SiR Interface, IEEE Trans. Dielectr. Electr. Insul. 26 (3) (2019) 689–697.

[5] B. Du, X. Zhu, L. Gu, H. Liu, Effect of surface smoothness on tracking mechanism in XLPE-Si-rubber interfaces, IEEE Trans. Dielectr. Electr. Insul. 18 (1) (2011) 176–181.

[6] E. Kantar, Longitudinal AC Electrical Breakdown Strength of Polymer Interfaces, Ph.D. thesis, NTNU (2019).

[7] E. Kantar, D. Panagiotopoulos, E. Ildstad, Factors Influencing the Tangential AC Breakdown Strength of Solid-Solid Interfaces, IEEE Trans. Dielectr. Electr. Insul. 23 (3) (2016) 1778–1788.

[8] M. Kato, Y. Nishimura, N. Osawa, Y. Yoshioka, H. Yanase, K. Okamoto, Effects of Compressive Force and Dielectric Materials on Contact Area for High-Pressure Region and Interfacial AC Breakdown Between Two Solid Dielectrics, in: Proc. 21st Int. Symp. HV Eng. (ISH), Springer Int., 2020, pp. 118–129.

[9] E. Kantar, S. Hvidsten, F. Mauseth, E. Ildstad, Longitudinal AC Breakdown Voltage of XLPE-XLPE Interfaces Considering Surface Roughness and Pressure, IEEE Trans. Dielectr. Electr. Insul. 24 (5) (2017) 3047–3054.

[10] E. Kantar, S. Hvidsten, E. Ildstad, Effect of Material Elasticity on the Longitudinal AC Breakdown Strength of Solid-Solid Interfaces, IEEE Trans. Dielectr. Electr. Insul. 26 (2) (2019) 655–663.

[11] E. Kantar, S. Hvidsten, F. Mauseth, E. Ildstad, A Stochastic Model for Contact Surfaces at Polymer Interfaces Subjected to an Electrical Field, Tribology Int. 127 (2018) 361–371.

[12] A. Almqvist, On the effects of surface roughness in lubrication, Ph.D. thesis, Luleå tekniska universitet (2006).

[13] B. Bhushan, X. Tian, A numerical three-dimensional model for the contact of rough surfaces by variational principle, ASME J. Tribol 118 (1996) 33–42.

[14] J. Greenwood, J. Williamson, Contact of nominally flat surfaces, in: Proc. Royal Soc. London A: Math., Phys. Eng. Sci., Vol. 295, The Royal Society, 1966, pp. 300–319.

[15] B. Bhushan, Analysis of the real area of contact between a polymeric magnetic medium and a rigid surface, J. Tribology 106 (1) (1984) 26–34.

[16] M. O'Callaghan, M. Cameron, Static contact under load between nominally flat surfaces in which deformation is purely elastic, Wear 36 (1) (1976) 79–97.

[17] H. Francis, Application of spherical indentation mechanics to reversible and irreversible contact between rough surfaces, Wear 45 (2) (1977) 221–269.

[18] H. Illias, G. Chen, P. L. Lewin, Modeling of partial discharge activity in spherical cavities within a dielectric material, IEEE Electr. Insul. Mag. 27 (1) (2011) 38–45.

[19] X. Chen, Y. Xu, X. Cao, S. M. Gubanski, Electrical treeing behavior at high temperature in XLPE cable insulation samples, IEEE Trans. Dielectr. Electr. Insul. 22 (5) (2015) 2841–2851.

[20] J. C. Fothergill, Filamentary electromechanical breakdown, IEEE Trans. Electr. Insul. 26 (6) (1991) 1124–1129.

[21] R. M. Eichhorn, Treeing in solid extruded electrical insulation, IEEE Trans. Electr.Insul. EI-12 (1) (1977) 2–18.

[22] J. H. Mason, Assessing the resistance of polymers to electrical treeing, IEE Proc. A: Phys. Sci. Meas. Instrum. Manage. Edu. Reviews 128 (3) (1981) 193–201.

[23] L. A. Dissado, J. C. Fothergill, Electrical degradation and breakdown in polymers, Vol. 9, IET, 1992.

[24] G. C. Crichton, P. W. Karlsson, A. Pedersen, Partial discharges in ellipsoidal and spheroidal voids, IEEE Trans. Dielectr. Electr. Insul. 24 (2) (1989) 335–342.

[25] F. Kreuger, Industrial high voltage: electric fields, dielectrics, constructions, Delft University Press, 1991.

[26] J. Kuffel, P. Kuffel, High voltage engineering fundamentals, Elsevier, 2000.

[27] Y. Gao, Y. Yuan, L. Chen, J. Li, S. Huang, B. Du, Direct fluorination induced variation in interface discharge behavior between polypropylene and silicone rubber under AC voltage, IEEE Access 6 (2018) 23907–23917.

[28] H. A. Illias, Measurement and simulation of partial discharges within a spherical cavity in a solid dielectric material, Ph.D. thesis, University of Southampton (2011).

[29] E. Kantar, E. Ildstad, A Novel Methodology to Monitor Partial Discharges in Microvoids at Solid-Solid Interfaces, in: IEEE Conf. Electr. Insul. Dielectr. Phen. (CEIDP), 2019, pp. 113–117.

[30] E. Kantar, F. Mauseth, E. Ildstad, Interfacial breakdown between dielectric surfaces determined by gas discharge, in: IEEE Conf. Electr. Insul. Dielectr. Phen. (CEIDP), 2017, pp. 556–559.

[31] D. R. Jones, M. F. Ashby, Engineering materials 1: An introduction to properties, applications and design, Butterworth-Heinemann, 2019, pp. 211–221.

[32] B. X. Du, J. Li, Interface charge behaviors between LDPE and EPDM filled with carbon black nanoparticles, IEEE Trans. Dielectr. Electr. Insul. 23 (6) (2016) 3696–3703.

[33] L. A. Dissado, Understanding electrical trees in solids: from experiment to theory, IEEE Trans. Dielectr. Electr. Insul. 9 (4) (2002) 483–497.

[34] S. M. Hasheminezhad, Tangential Electric Breakdown Strength and PD Inception Voltage of Solid-Solid Interface, Ph.D. thesis,

Norwegian Uni. Sci. Tech. (2016).

[35] K. C. Kao, Dielectric phenomena in solids, Academic press, 2004.

[36] IEC 62539 First Edition 2007-07 IEEE 930, IEC/IEEE Guide for the Statistical Analysis of Electrical Insulation Breakdown Data (Adoption of IEEE Std 930-2004) (2007) 1–53.